Landslides, threshold slopes, and the survival of relict ter-rain in the wake of the Mendocino Triple Junction
Georgina L. Bennett et al.

DATA REPOSITORY

REGIONAL GEOLOGY

The northern California Coast Ranges are composed the Franciscan Complex, a penetratively sheared set of metasedimentary rocks forming an accretionary prism. The Franciscan complex is subdivided into three broad belts that young to the west: the Eastern, Central and Coastal belts, reflecting the cumulative accretion of oceanic sediments to western North America (McLaughlin et al., 2000). Our study area encompasses the Central and Coastal belts, described further here. The Central belt consists predominantly of Franciscan Mélange (KJf in Fig. 1A and DR1), which is a penetratively sheared, Jurassic-Cretaceous, argillitic mélange embedded with blocks of more coherent sandstone and shale turbidites and occasional blocks of metabasalt and others. The younger Coastal belt can be divided into several structural terranes. Most relevant for our study area are the Yager terrane (EP in Fig. DR1), and Coastal terrane (TK in Fig. DR1). The Yager terrane is composed predominantly of Paleocene to Eocene argillite, sandstone and conglomerate that vary from well bedded to sheared. The Coastal terrane is compositionally similar to the Yager, but is more penetratively disrupted and sheared and contains some additional lithologies such as blocks of basalt. Rocks of the Coastal terrane span the late Cretaceous to Pliocene.

METHODS

Landslide mapping

Fisher et al. (2012), demonstrated the accuracy of Google Earth (GE) for mapping landslides in Haiti, observing that landslides mapped using GE in New Zealand match up very well with those previously mapped from multiple individually orthorectified aerial photographs. They promote the use of GE for several earth science applications including landslide mapping, especially for large areas for which commercial imagery is expensive and time consuming to process. We

followed suit by mapping ~3000 landslides in our study area using GE. We used mostly 2012 GE aerial photographs, the most recent imagery available at the time of mapping to identify landslides, calibrating our mapping visually on 69 earthflows mapped by Mackey and Roering (2011) in the Eel catchment. We used a suite of older imagery available in GE (Table DR1) to assess the activity of earthflows and where possible measure earthflow velocity from displaced features (Fig. DR3; Fig. DR4). Dormant earthflows have a number of features also characteristic of active earthflows such as gullies and a lower density of vegetation, but critically do not display any recent surface disturbance such as scarps and had no detectable movement. Following completion of our landslide inventory, 2014 GE aerial imagery became available. We used this to check our inventory especially in areas affected by wildfire smoke in 2012 imagery.

Landslide erosion rate calculation

Earthflow depth was calculated from mapped area as $Z=\alpha A^{\gamma}$, where Z is landslide depth, α is a fit parameter, A is area, and γ is the power-law exponent (Handwerger et al., 2013). We used parameter values of $\gamma=0.29$ (0.22, 0.36) and $\alpha=0.46$ (0.051, 0.87) calculated by Handwerger et al. (2013) using a non-linear least squares regression ($R^2=0.45$) of the depths and areas of 69 landslides in the Eel River measured by Mackey and Roering (2011). We calculated the empirical scaling relationship between area and width measurements of the same 69 landslides of Mackey and Roering (2011) using non-linear least squares regression. The relationship takes the form of $W=\delta A^{\beta}$, where $\delta=0.86$ (0.52, 1.19) and $\beta=0.44$ (0.41, 0.47), with an $R^2=0.85$ (Fig. DR5). We used this relationship to calculate the earthflow width from mapped area. We converted debris slide area into volume using the empirical scaling relationship between landslide area and volume, $V=\alpha A^{\delta}$, and using parameter values for soil-based slides in northern California presented in Larsen et al. (2010) of $\alpha= -0.49\pm0.02$ and $\delta=1.19\pm0.008$. Finally, erosion

47 rates were calculated by first converting flux to a sediment yield (metric t km^{-2} yr^{-1}) assuming a
48 density of earthflow colluvium of 2.1 g cm^{-3} (Kelsey, 1978; Mackey et al., 2009). This is then
49 converted into a rock erosion rate assuming a bedrock density of 2.5 g cm^{-3} (Mackey and
50 Roering, 2011) and given an averaging area of either swaths along the MCC transect (Fig. 2, Fig.
51 DR6), swaths along individual catchments (e.g. Fig. 4) or subcatchments (Fig. 3, Fig. DR8).

52 **Uncertainty in earthflow erosion rates**

53 Uncertainty in earthflow erosion rates may originate from human mapping error, the scaling
54 relationships used to convert earthflow area into width and depth, uncertainty in parameter
55 values within these scaling relationships, and lastly in the velocity measurements. For other
56 limitations in our approach see Mackey and Roering (2011). We account for uncertainty in
57 scaling parameter values and our velocity measurements, whilst recognizing that the other two
58 sources may also contribute to uncertainty. We produce three erosion rate estimates, a mean rate
59 using mean values of scaling parameters and not considering uncertainty in earthflow velocity,
60 and upper and lower rates bracketing this that do consider these uncertainties. We account for
61 uncertainty in area-width and area-depth scaling parameter values using the 5 and 95%
62 confidence interval values from the regressions of width and depth with area described above.
63 We made an assessment of the average error of our velocity measurements by measuring the
64 displacement of stable features, mainly buildings, between imagery used to measure earthflow
65 velocity. We measured displacements of 141 stable points between multi-temporal imagery
66 arriving at an average annual displacement (error) of 0.2 m yr^{-1}, which is a lower detection limit
67 for active earthflows. In the calculation of the upper erosion rate we add this error to each
68 velocity measurement and in the calculation of lower erosion rate we subtract it.

69

Uncertainty in debris slide erosion rates

Uncertainty in our debris slide erosion rates may originate from human mapping error, the scaling relationship used to convert debris slide area into volume, uncertainty in the parameter values in the scaling relationship, and the number of years over which debris slide flux is averaged to obtain an annual flux. Here we account for uncertainty in parameter values in the area-volume scaling relationship presented above and in the estimated age of the debris slide inventory. We use the mean and 5/95% confidence interval parameter values in area-volume scaling in our median, lower and upper erosion rate estimates respectively. We consider two possible end members of 10 and 30 years for debris slide inventory age based on a visual assessment of debris slide longevity in the landscape (e.g., Larsen and Montgomery, 2012) (Fig. DR2). We found evidence of some debris slides that are almost completely re-vegetated within ~10 years (e.g., Fig. DR2A-C). However, a number of slides that occurred before the start of our study period ~1990 are still clearly visible (e.g., Fig. DR2D,E). Considering uncertainty in these age estimates we produce two estimates of debris slide erosion rates and total landslide erosion rates.

Channel analysis

We adapted Topotoolbox 2 (Schwanghart and Scherler, 2014) to extract normalized channel steepness index (k_{sn}) for the channel network from an 10 m USGS National Elevation Dataset (NED) digital elevation model (Wobus et al., 2006). To reduce noise from DEM artifacts, we smoothed channel elevations with a 100 m long moving filter. The filter we used ("filtfilt" in Matlab) reproduces more faithful elevations near confluences than the commonly used boxcar filter (e.g., Wobus et al., 2006), which can produce steps (or virtual hanging valleys) at tributary junctions. Normalized channel steepness index was calculated within a 1000 m long moving

93 window and a reference concavity of 0.55 for the Eel River basin following Shi (2011).
94 Knickpoints were identified using an automated method that scanned every channel in the stream
95 network, arbitrarily designated as cells on the DEM with upstream drainage areas >1 km^2.
96 Knickpoints were identified wherever the ratio between downstream and upstream k_{sn} averaged
97 within two serial windows (each 2 km long) exceeded a factor of two. This ratio was determined
98 to be the minimum ratio associated with most migratory knickpoints (22 out of 23) manually by
99 Shi (2011), while at the same time avoiding a large fraction of likely anchored knickpoints either
100 pinned to lithologic contacts between rock units with contrasting erodibilities or created by
101 landslides (13 out of 29 static knickpoints steepen by a factor less than 2). Where adjacent DEM
102 cells along the channel all met this criterion, the cell between two windows with the largest
103 downstream-upstream ratio was marked as the knickpoint. To further avoid false positives
104 associated with static knickpoints, we conservatively avoided knickpoints within 0.5 km
105 (Euclidean distance) of a mapped lithologic contact (Saucedo et al., 2000).

106 **FURTHER DISCUSSION**

107 Lock et al. (2006) propose a modified version of Furlong and Govers' (1999) 'single hump'
108 isostatic uplift model (Fig.2A,B), termed the 'double hump' model (Lock et al., 2006, their
109 figure 5) that incorporates an additional component of flexure and dynamic topography in the
110 modeled uplift field. Lock et al. (2006) suggest that this model can better explain the modern day
111 regional topography and planform drainage pattern. However, as they acknowledge, they lack a
112 rigorous test of the uplift field based on geomorphic erosion rates. Our study is the first to offer
113 these constraints in the form of regional landslide erosion rates and channel steepness indices.
114 Our data are consistent with a broad zone of increased uplift due to crustal thickening alone

(Furlong and Govers, 1999) and does not require that a double humped pattern be invoked (Fig. DR6C).

Our analysis of landslide erosion rates sheds new light on the interpretation of cosmogenic nuclide erosion rates in the South Fork Eel (Willenbring et al., 2013). We observe that landslide erosion rates in subcatchments of the SF Eel (Fig. 2E; Fig. DR8A) increase upstream, in contrast to cosmogenic erosion rates. Our data suggest that the downstream increase in cosmogenic erosion rate results from the increased contribution of sediment from landslides, particularly earthflows, from adjusting tributaries within the highly Franciscan Mélange, and not just from a decreasing area of relict terrain as Willenbring et al. (2013) suggest.

FURTHER REFERENCES

Fisher, G. B., Amos, C. B., Bookhagen, B., Burbank, D. W., and Godard, V., 2012, Channel widths, landslides, faults, and beyond: The new world order of high-spatial resolution Google Earth imagery in the study of earth surface processes: Geological Society of America Special Papers, v. 492, p. 1–22, doi:10.1130/2012.2492(01).

Mclaughlin, R. J., Ellen, S. D., Blake, J. M. C., Jayko, A. S., Irwin, W. P., Aalto, K. R., … Clark, J. S. H. (2000). Geology of the Cape Mendocino, Eureka, Garberville, and Southwestern part of the Hayfork 30 x 60 Minute Quadrangles and Adjacent Offshore Area, Northern California. Miscellaneous Field Studies MF-2336, 2000–2000.

Jennings, C. W, 1977, Geologic map of California, Geologic Data Map Series Map 2, scale 1:750000. Sacramento, California.

Saucedo, G. J., Bedford, D. R., Raines, G. L., Miller, R. J., Wentworth, C. M. (2000). GIS Data

for the Geologic Map of California. Sacramento, California.

Schwanghart, W., and Scherler, D., 2014, Short Communication: TopoToolbox 2 – MATLAB-based software for topographic analysis and modeling in Earth surface sciences: Earth Surface Dynamics, vol. 2, no. 1, p. 1–7, doi:10.5194/esurf-2-1-2014.

Table DR1. Google Earth imagery used to map landslides and measure earthflow velocities.

Date	Image type	Source
8/24/1988	Digital orthophoto quandrangles	USGS
5/31/1993	Digital orthophoto quandrangles	USGS
6/11/1993	Digital orthophoto quandrangles	USGS
6/12/1993	Digital orthophoto quandrangles	USGS
8/11/1998	Digital orthophoto quandrangles	NAPP
11/20/2004	Satellite image	Digital Globe
6/11/2005	Digital orthophoto quandrangles	USDA Farm Service Agency
5/3/2006	Satellite image	Digital Globe
5/24/2009	Satellite image	USDA Farm Service Agency
4/24/2010	Digital orthophoto quandrangles	USDA Farm Service Agency
8/23/2012	Aerial photo	Google
7/9/2012	Aerial photo	Google
7/10/2012	Aerial photo	Google
5/28/2014	Aerial photo	Google
5/30/2014	Aerial photo	Google

Table DR2. Landslide erosion rates broken down by landslide type. Mean erosion rates are those calculated using mean values of scaling parameters in earthflow area-depth, area-width and debris slide area-volume relationships, and not considering uncertainty in velocity measurements. Upper erosion rates are calculated using the 95% parameter values in geometrical scaling relationships of earthflows and debris slides and upper velocity estimates of earthflows. Lower erosion rates are calculated using the 5% parameter values in geometrical scaling relationships and lower velocity estimates of earthflows. The mean value we report in the text is the mean of the values in bold, i.e. 0.18 ± 0.04 mm yr^{-1}.

	Rock erosion rate (mm yr^{-1})							
Study area	Active earth flow	Dormant earth flow	Total earth flow	Debris slide 30yr	Debris slide 10 yr	Total landslide erosion rate (10 yr)	Total landslide erosion rate (30 yr)	Total landslide flux (10 yr) (t km^{-2} yr^{-1})
Upper	0.383	0.449	0.832	0.047	0.141	0.972	0.879	2042
Mean	0.056	0.043	0.098	0.040	0.120	**0.218**	**0.138**	457.8
Lower	0.001	0.001	0.001	0.035	0.105	0.106	0.036	223.2
KJf only								
Upper	0.649	0.763	1.413	0.054	0.163	1.575	1.467	1575
Mean	0.094	0.072	0.166	0.046	0.138	0.304	0.212	304.4
Lower	0.001	0.001	0.002	0.040	0.121	0.123	0.043	123.3
Eel only								
Upper	0.455	0.643	1.098	0.067	0.200	1.297	1.164	2725
Mean	0.064	0.061	0.125	0.057	0.170	0.295	0.181	618.6
Lower	0.001	0.001	0.002	0.050	0.149	0.151	0.051	316.2

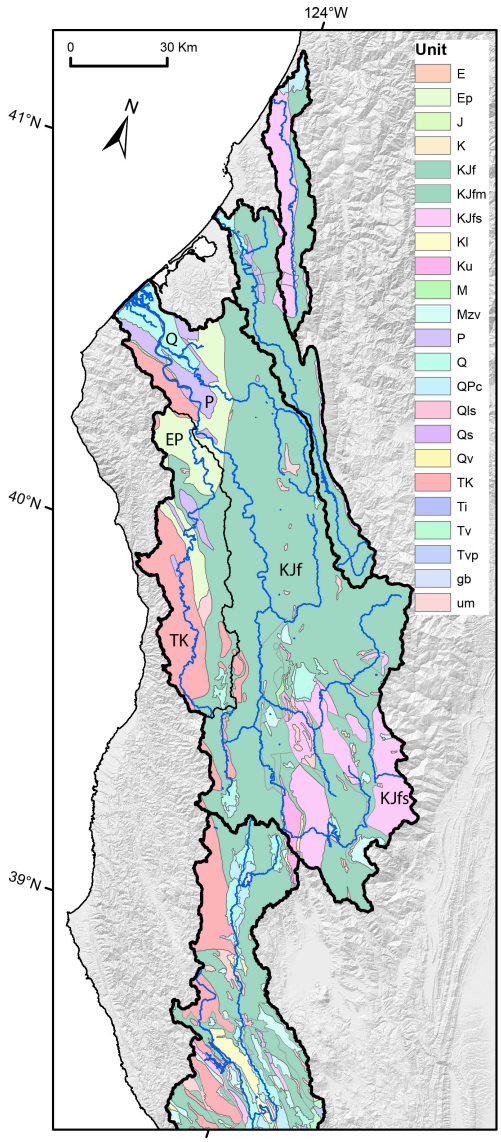

Figure DR 1 – Geological map of the Franciscan Complex adapted from Saucedo et al. (2000), clipped to our four study catchments. The South Fork Eel catchment within the Eel Catchment is also delineated. The main units referred to in the DR are indicated.

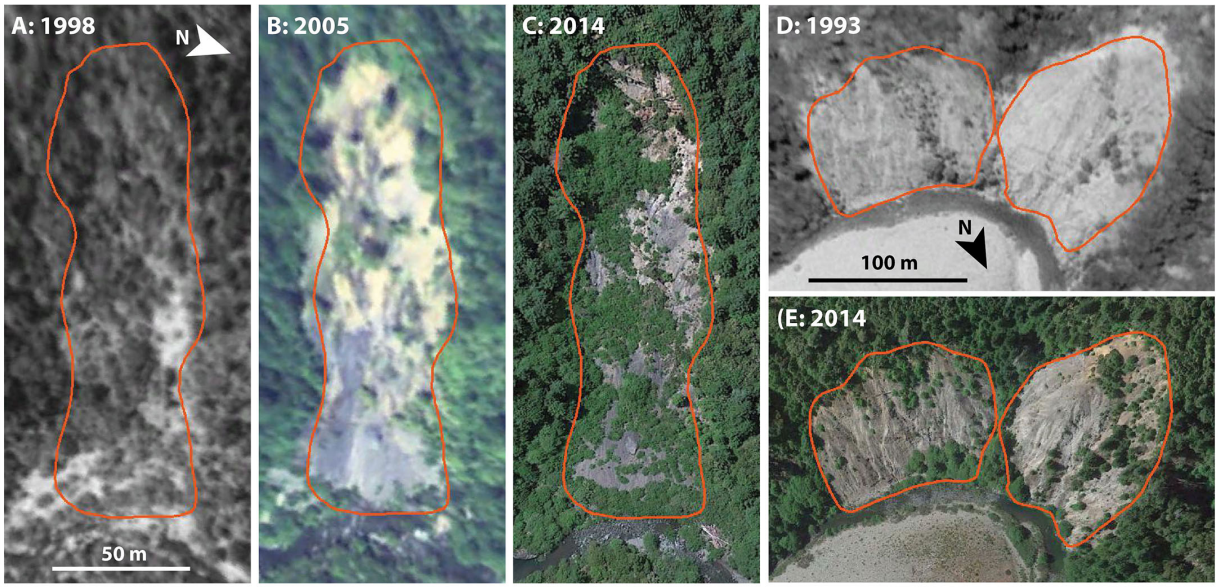

Figure DR2. Examples of debris slides and their re-vegetation. A – C show a debris slide that occurred sometime between 1998 and 2005 and is mostly re-vegetated by 2014, i.e. within ~10 years. D–C show a debris slide that occurred prior to 1993 and is still clearly exposed in 2014, suggesting a re-vegetation time longer than 20 years.

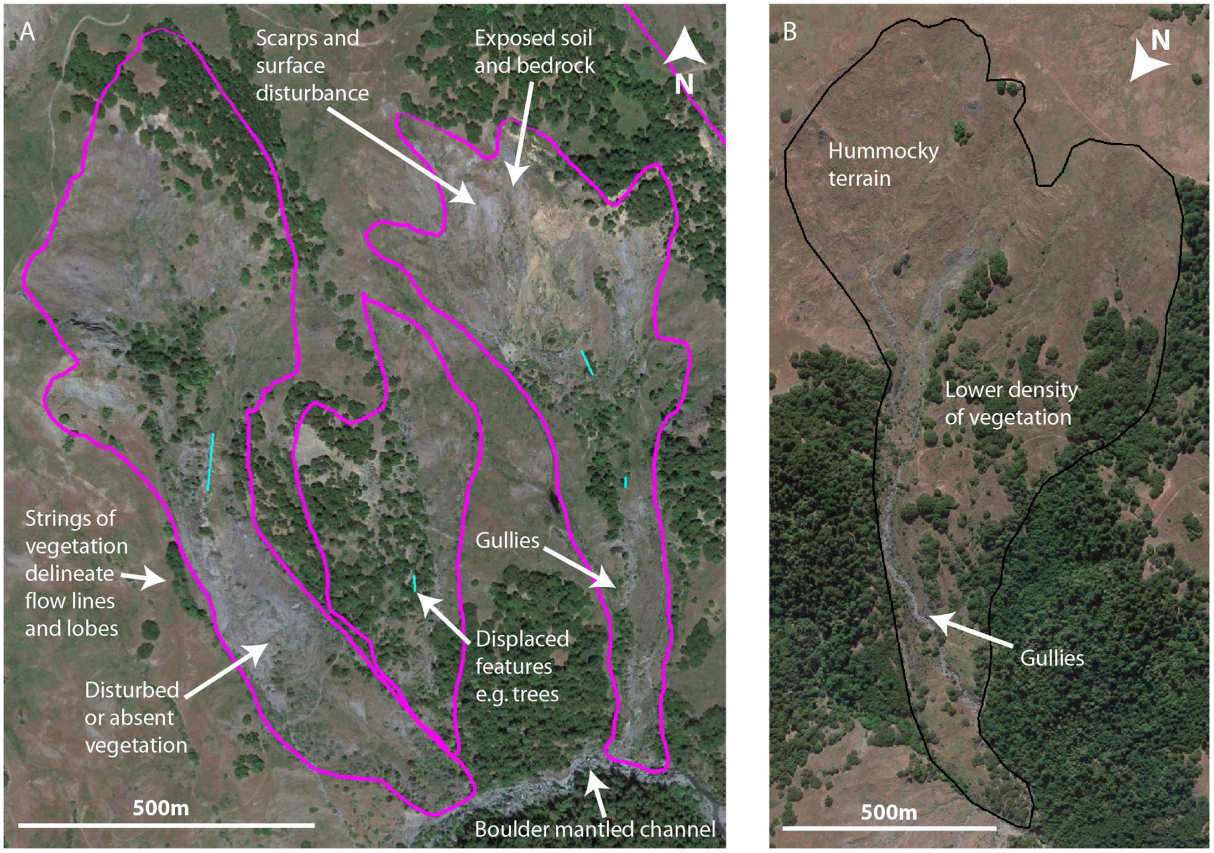

163

164 Figure DR3. A: Active earthflows along the Van Duzen tributary of the Eel River showing

165 characteristic morphology and disturbance features used to map active earthflows from Google

166 Earth imagery. B: A characteristic dormant earthflow in the Eel catchment.

167

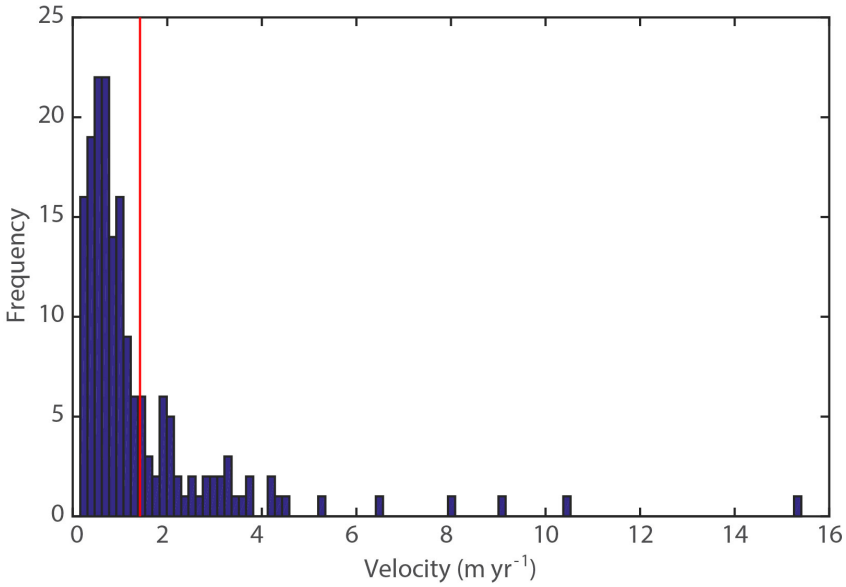

168

169 Figure DR4. Histogram of measured earthflow velocities above the detection limit of 0.2 m yr^{-1}.

170 Mean earthflow velocity of 1.44 m yr^{-1} is marked in red.

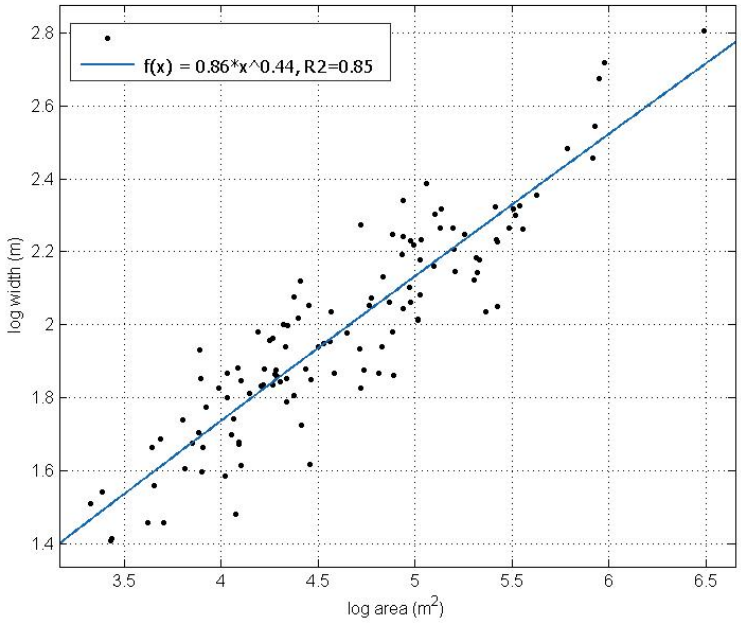

171

172 Figure DR5. Empirical scaling relationship between width and area of 69 earthflows mapped by

173 Mackey and Roering (2011) in the Eel. See text for more details.

174

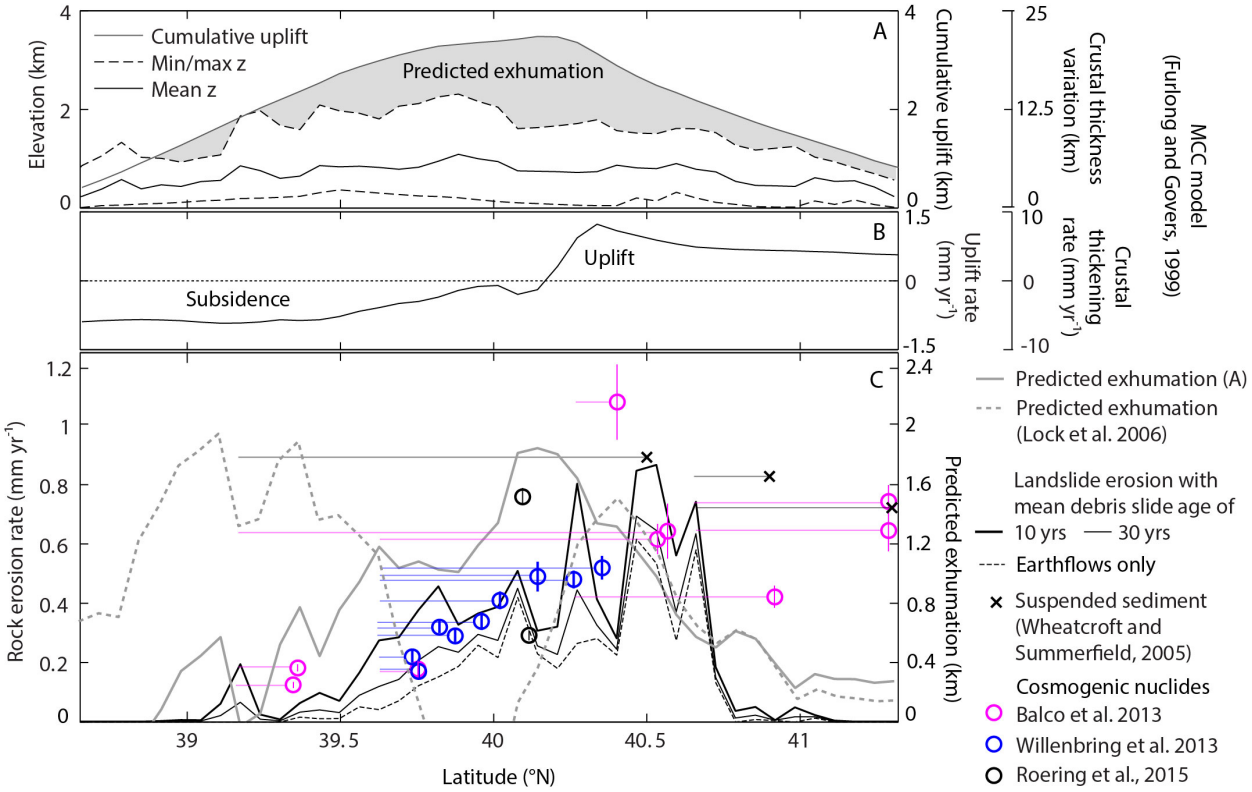

Figure DR6. Expanded version of Fig. 2 showing extra details in derivation of uplift curves and landslide erosion rate. A: Observed elevation and modeled cumulative uplift as calculated from MCC-modeled crustal thickness variation (Furlong and Govers, 1999) assuming local isostasy and a typical density variation between the crust and the mantle (Lock et al., 2006). Crustal thickness variation is calculated by Furlong and Govers (1999) by integrating their MCC-modeled crustal thickening rate shown in panel B. B: Predicted uplift rate calculated from the MCC-modeled crustal thickening rate assuming local isostasy and a typical density variation. C: Swath-averaged landslide erosion rates within KJf compared to cosmogenic nuclide erosion rates, suspended sediment erosion rates and predicted exhumation as depicted in panel A, and predicted exhumation based on the 'double-hump' model of Lock et al. (2006). The tails on cosmogenic and suspended sediment erosion rates depict the upstream area over which these rates integrate.

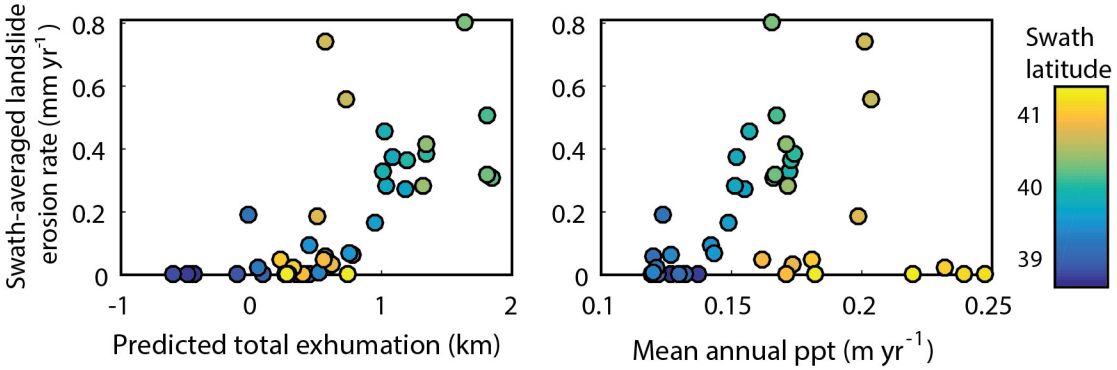

188
189

190 Figure DR 7 – A: Relationship of swath-averaged landslide erosion rate in KJf with predicted

191 exhumation (see Fig DR6) and B: with mean annual precipitation obtained from PRISM for 1981

192 - 2010.

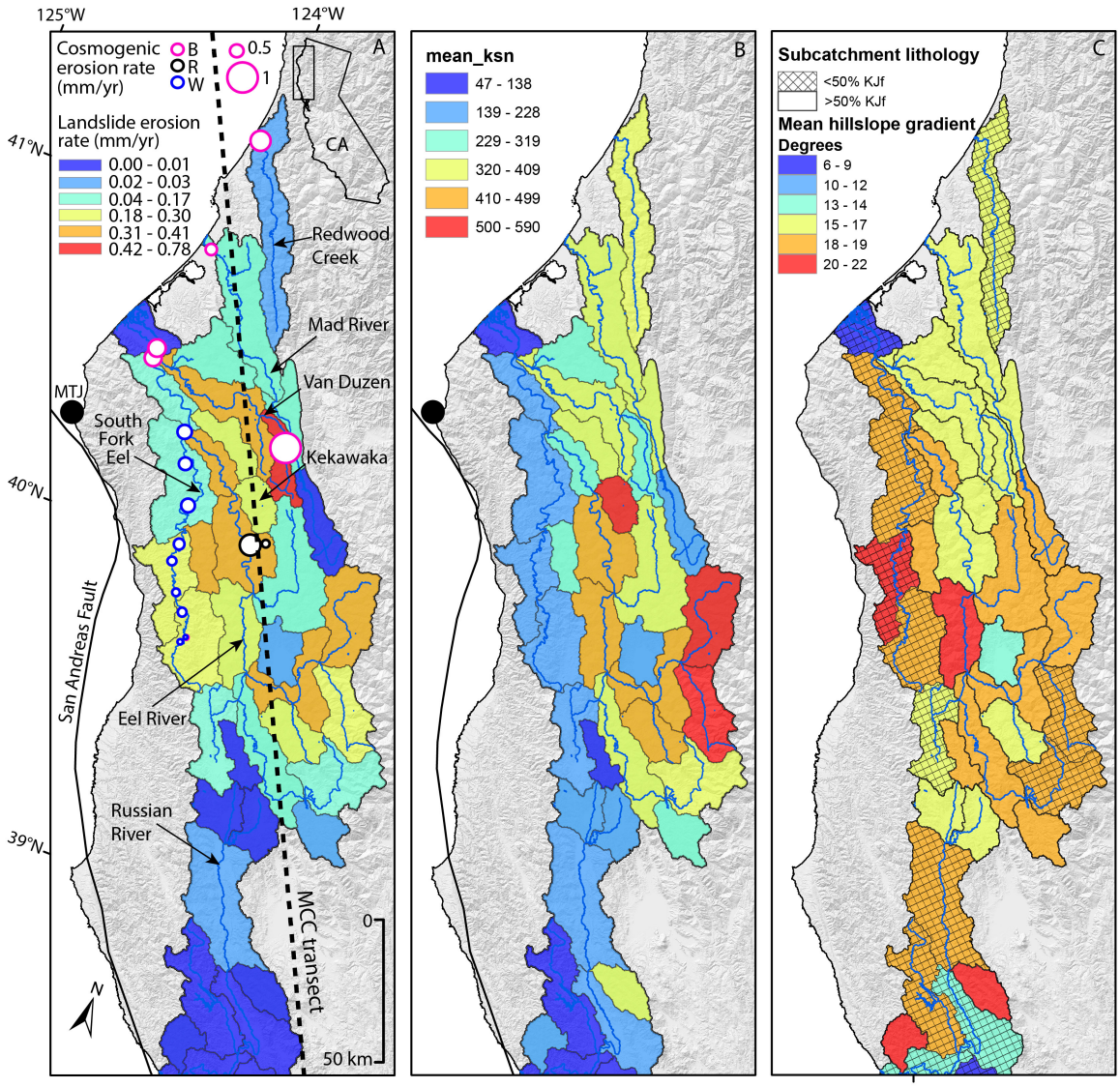

193

194 Figure DR8. A: Landslide erosion rates measured in this study averaged by USGS-defined

195 subcatchments within the 4 study catchments spanning the MCC model domain (Redwood, Mad,

196 Eel and Russian) for comparison with published cosmogenic nuclide erosion rates (B = Balco et

197 al. (2013); R = Roering et al. (2015); W = Willenbring et al. (2013)). B: Mean k_{sn} by

198 subcatchment. C: Mean hillslope gradient by subcatchment. Subcatchments with >50% KJf

199 lithology, used in Fig. 3, are highlighted (no cross-hatching).

200

201

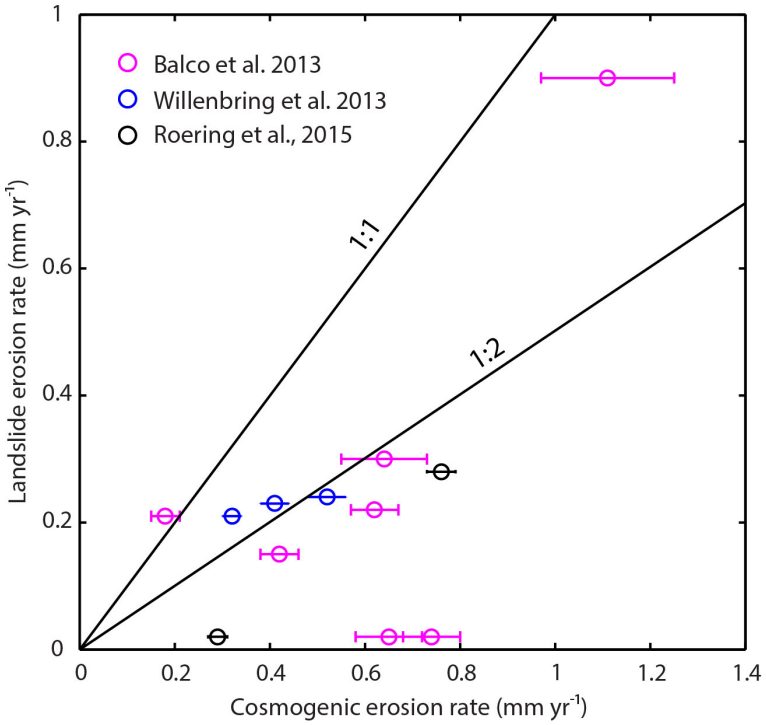

202

203 Figure DR9. Landslide erosion rates averaged by (sub)catchment areas corresponding to

204 cosmogenic nuclide erosion rates. Landslide erosion rate tend to lie on the 1:2 line with

205 cosmogenic erosion rates.

206

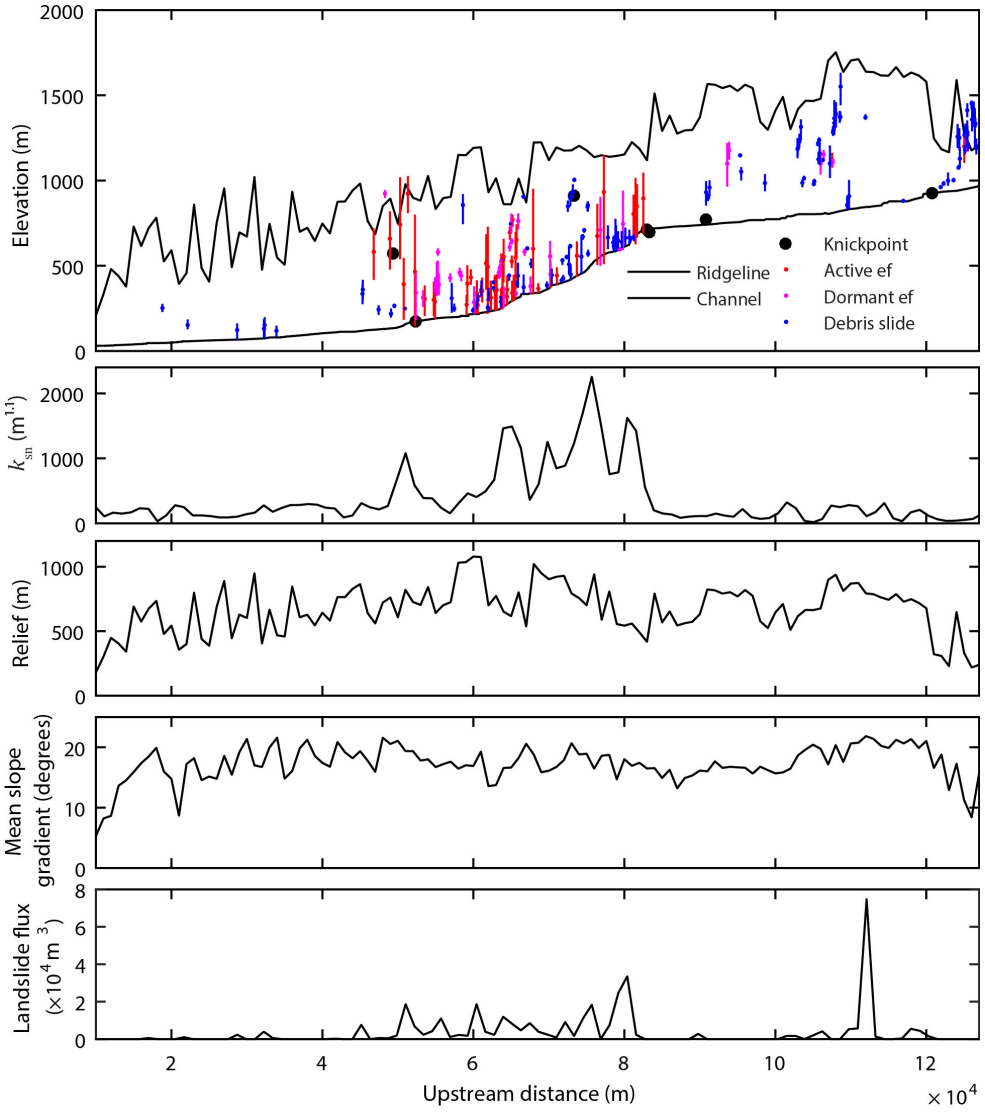

Figure DR 10 – Landslides and topography along the Van Duzen, KJf-dominated tributary of the Eel (see Fig. DR8 for location).

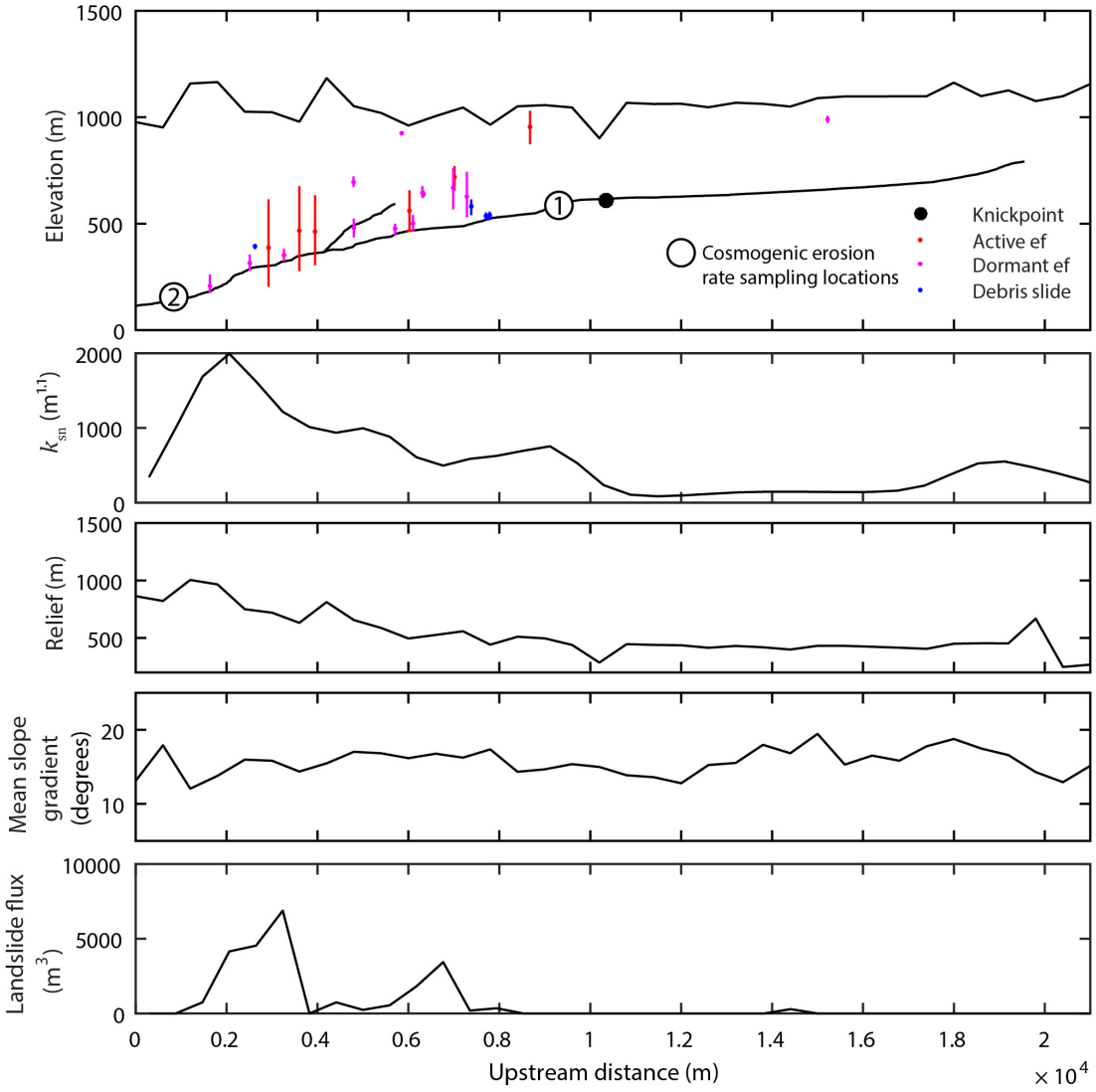

210

211 Figure DR11 – Landslides and topography along the Kekawaka, KJf-dominated tributary of the

212 Eel (see Fig. DR8 for location). 1 and 2 refer to cosmogenic erosion rate labels in Fig. 3C.

Figure DR12 – A: Megaclasts of >10 m along the Kekawaka landslide-lined knickzone (Fig. DR11). B: Boulder-mantled earthflow toes along the main Eel channel near the junction of the Kekawaka.